Research Square

Preprints are preliminary reports that have not undergone peer review.
They should not be considered conclusive, used to inform clinical practice,
or referenced by the media as validated information.

A Novel Ferro-Aging-Related Gene Signature for Prognosis and Targeted Drug Prediction in Cervical Cancer

Zhengchao Yan
Nanxi Mountain Hospital
Sijuan Tang
Affiliated Hospital of Guilin Medical College
Naqiu Yin
Nanxi Mountain Hospital
Ying Wan
Nanxi Mountain Hospital
Yufei Pan
Nanxi Mountain Hospital
Yue Li
Nanxi Mountain Hospital
Ximei Huang
Nanxi Mountain Hospital
Liwu Zhang
Nanxi Mountain Hospital
Jianlin Chen
cjl801900@163.com

Nanxi Mountain Hospital

Article

Keywords: cervical cancer, ferro-aging, machine learning, SHAP, single-cell, spatial transcriptomics, drug screening

Posted Date: July 15th, 2026

DOI: https://doi.org/10.21203/rs.3.rs-9957206/v1

License: This work is licensed under a Creative Commons Attribution 4.0 International License.
Read Full License

Additional Declarations: No competing interests reported.

Version of Record: A version of this preprint was published at Scientific Reports on November 4th, 2026. See the published version at https://doi.org/10.1038/s41598-026-78172-3.

A Novel Ferro-Aging-Related Gene Signature for Prognosis and Targeted Drug Prediction in Cervical Cancer

Zhengchao Yan[1+], Sijuan Tang[2+], Naqiu Yin[1], Ying Wan[1], Yufei Pan[3] , Yue Li[1], Ximei Huang[1] ,Liwu Zhang[4*], Jianlin Chen[1*]

[1]Department of Clinical Laboratory, Nanxishan Hospital of Guangxi Zhuang Autonomous Region, Guilin 541002, China.

[2]Department of Laboratory Medicine, The Second Affiliated Hospital of Guilin Medical University, Guilin 541100, China.

[3]Department of Oncology, Nanxishan Hospital of Guangxi Zhuang Autonomous Region, Guilin 541002, China.

[4]Department of Obstetrics and Gynecology, Nanxishan Hospital of Guangxi Zhuang Autonomous Region, Guilin 541002, China.

[+] These authors contributed equally to this work and share first authorship.

*** Correspondence author:**Jianlin Chen E-mail: cjl801900@163.com. Liwu Zhang E-mail: 923567063@qq.com.

Competing Interests: The authors declare that they have no known competing financial interests or personal relationships that could have appeared to influence the work reported in this paper.

Authors' information:

Department of Clinical Laboratory, Nanxishan Hospital of Guangxi Zhuang Autonomous Region, Guilin 541002

Zhengchao Yan, Naqiu Yin, Ying Wan, Yue Li, Ximei Huang & Jianlin Chen

Department of Laboratory Medicine, The Second Affiliated Hospital of Guilin Medical University, Guilin 541100, China.

Sijuan Tang

Department of Oncology, Nanxishan Hospital of Guangxi Zhuang Autonomous Region, Guilin 541002, China.

Yufei Pan

Department of Obstetrics and Gynecology, Nanxishan Hospital of Guangxi Zhuang Autonomous Region, Guilin 541002, China.

Liwu Zhang

Abstract

Objective: Cervical cancer (CESC) remains a leading cause of cancer-related mortality in women. Recent studies have identified ferro-aging as a genuine biological pathway in primates, representing an iron-dependent metabolic process. However, cellular ageing and the decline in overall physiological function play a crucial role in tumour progression. Based on this, we have established a prognostic model related to ferro-aging and evaluated its predictive and diagnostic value in cervical cancer.

Methods: We integrated data from the The Cancer Genomics Atlas (TCGA), the Gene Expression Online Resource (GEO) and single-cell RNA sequencing datasets. Following the identification of ferro-aging-

related gene (FARGs) based on the literature, we constructed a prognostic model using machine learning algorithms and analysed model features via Shapley-based interpretability (SHAP) analysis. The Scissor algorithm was employed to evaluate cell populations associated with high- and low-risk groups. Studies on intercellular communication and spatial transcriptomics revealed the process of tumour microenvironment remodelling. Finally, potential therapeutic compounds were identified through AI-assisted virtual screening and molecular docking.

Results: A total of eight FAR model genes were ultimately identified: *DUOX1, E2F1, IL1B, KEAP1, MAP3K14, SLAMF8, TFRC and TNFAIP3*. This study constructed and validated a novel risk profile model comprising these eight ferro-aging-related genes; this model demonstrated moderate prognostic discriminatory power in both internal and external cohorts, with the tumour microenvironment in the high-risk group exhibiting an immunosuppressive state. Using single-cell RNA sequencing to assess cellular heterogeneity, macrophages, epithelial cells and CD8+ T cells were identified as key factors in CESC progression. Pseudotime analysis was performed to visualize the expression levels of FARGs along the pseudotime axis and explore how FARGs participate in the dynamic process of EndMT. Spatial transcriptomics was employed to map the distribution and expression of FARGs within epithelial cells in the tumour microenvironment. Intercellular communication intensity was increased in the low-risk group, with epithelial cells in this group signalling to macrophages via the APP-CD74 pathway. Drug screening indicated that BRD-A56371469 is likely to bind to DUOX1.

Conclusions: The FARG signature is a robust independent prognostic indicator for CESC. The integrated pipeline offers insights into ferro-aging biology and suggests novel therapeutic candidates.

Keywords: cervical cancer; ferro-aging; machine learning; SHAP; single-cell; spatial transcriptomics; drug screening

1.Introduction

Cervical cancer (CESC) is the fourth most common malignant tumour among women worldwide and one of the leading causes of cancer-related deaths in women; its incidence remains particularly high in developing countries[1, 2]. Although the widespread use of human papillomavirus (HPV) vaccines and early screening methods have significantly improved the prevention and control of cervical cancer, the prognosis for patients with advanced disease remains poor, and incidence and mortality rates continue to rise, placing a heavy clinical and economic burden on both individual patients and the healthcare system[3, 4]. Treatment for this disease typically involves surgery, chemotherapy and long-term monitoring, with treatment costs remaining high; recurrence and metastasis are the primary causes of treatment failure[5]. Therefore, identifying new biomarkers, gaining a deeper understanding of their molecular mechanisms, and developing targeted therapeutic strategies are of significant clinical importance[6].

Various treatment limitations highlight the need to investigate the molecular mechanisms underlying cervical cancer and to screen for clinically useful biomarkers to aid in diagnosis, prognostic assessment and optimisation of clinical management[7, 8]. Significant tumour heterogeneity, persistent activation of inflammatory signals and the formation of an immunosuppressive tumour microenvironment are key factors contributing to clinical challenges; these factors can lead to treatment resistance and tumour recurrence.Single-cell RNA sequencing has now become a primary tool for understanding disease mechanisms[9]. For patients with cervical cancer, a disease characterised by intricate pathogenesis, cutting-edge research methods are essential to thoroughly elucidate the tumour immune

microenvironment and cellular heterogeneity[10]. Current research is gradually unravelling the complex molecular characteristics of cervical cancer, confirming that senescence plays a key role in tumour progression; as a component of the tumour microenvironment attracting significant attention, research in this area is gaining increasing momentum[11].

Recent studies have revealed that “Ferro-aging” constitutes a genuine, modifiable biological pathway in primates; it is an iron-dependent metabolic programme driven primarily by the ACSL4-dependent iron-lipid axis[12]. This process accelerates up the gradual deterioration of organ function in addition to directly encouraging cellular senescence. This senescence may lead to conditions like neurological, metabolic, and heart disease[13]. At the cellular level, as senescent cells proliferate, the senescence-associated secretory phenotype (SASP) they release further interferes with intercellular communication, causes continuous sterile inflammation, and hinders tissue regeneration and repair while toxic chemicals continue to construct up[14, 15].

Cellular senescence and cancer have a very intricate relationship.. Cellular senescence is thought to be an anti-tumor mechanism that protects against the development of cancer; injured cells go into a senescent circumstance to stop cells from dividing further, which stops the growth of tumors[16, 17]. On the other hand, the senescence-associated secretory phenotype stimulates the growth, invasion, and metastasis of tumors by acting on surrounding healthy cells; the recurrent build-up of these secretions also causes chronic tissue inflammation, which further encourages the development of tumors[18]. Depending on the milieu in which they live, senescent cells release different cytokines that have both pro- and anti-tumor affecting effects[19].

Ferro-aging is a lipid peroxidation-driven, iron-triggered, ACSL4-regulated senescence process that differentiates in some ways from ferroptosis[12]. Nevertheless iron metabolism is the primary cause of both. Ferroptosis can protect the body from cervical cancer by eliminating pathogens and slowing the illness's advancement. However, in more advanced stages of the disease, ferroptosis may worsen tissue damage and hasten the disease's progression[20]. However, there is still insufficient amount of systematic study on the expression profiles, prognostic implications, and regulatory responsibilities of ferro-aging-related genes in the cervical cancer tumor microenvironment.

Ferro-aging-related genes (FARGs) are systematically screened to utilize multi-omics data (which may include transcriptomics, single-cell RNA sequencing, and spatial transcriptomics), a FARG-based prognostic model for cervical cancer is established and validated. These model features are analyzed using machine learning and artificial intelligence technologies, their associations with immune infiltration, intercellular communication, and spatial heterogeneity are explored, and potential therapeutic compounds are investigated in the hope to provide new targets and protocols for the precision treatment of cervical cancer.

2. Materials and methods

2.1 Data download and processing

All data used in this study were publicly available and freely accessible. Expression profiles and survival data for cervical cancer samples were downloaded from the The Cancer Genome Atlas (TCGA) database and the Gene Expression Online Resource (GEO); expression profile data were transformed using log2(TPM + 1) for further analysis. The TCGA-CESC dataset comprises 309 cervical cancer samples, which served as the training set for constructing the FARG; the GSE44001 dataset served as an independent validation cohort, comprising 300 cervical cancer samples with clinical information. In addition, we retrieved single-cell RNA sequencing (scRNA-seq) data for one CESC tumour and one normal tissue from GSE168652 to visualise the gene expression profiles of each cell cluster. Sets of ferro-

aging-related genes were extracted from published literature[12]. Spatial transcriptomic data were obtained from 10×Visium. This study strictly adheres to the data access guidelines of each database; as the research data were primarily derived from publicly available datasets, no additional ethical review was required.

2.2 Cox Regression and Consensus Clustering

We applied univariate Cox regression and consensus clustering analyses on the TCGA-CESC cohort to clarify the biological characteristics of associated putative prognostic factors and the possible prognostic features associated with FARGs in CESC. First, using the "survminer" package in R, univariate Cox regression was used to assess potential predictive signs based on clinical data from patients with cervical cancer, with a significance threshold of $P < 0.05$. Additionally, CESC patients were separated into high- and low-risk groups utilizing the R package "ConsensusClusterPlus".

2.3 Interpretable Machine Learning and Prognostic Model Construction

The filtering criterion for the univariate Cox analysis was set at CoxPfilter = 0.05. Genes were iterated through to identify FAR genes associated with prognosis, and expression data for univariate significant genes were extracted. To identify prognostic features associated with FARGs, we established an integrated analysis workflow comprising ten machine learning algorithms: random survival forest (RSF), elastic network (Enet), Lasso, Ridge, stepwise Cox, CoxBoost, Partial Least Squares Regression for Cox (PLS-RCOX), Supervised Principal Components (SuperPC), Generalised Boosted Regression Modelling (GBM), and Survival Support Vector Machine (Survival-SVM). Based on the maximum mean C-index across the training and testing sets, we assessed these models and classified 101 distinct model configurations. The genes linked with FAR prognosis were chosen from the top-ranked model. The Shapley Additive Explanations (SHAP) approach was used for model interpretability analysis in order to clear the estimation mechanisms of the best machine learning model. This method increases confidence in the predictions by giving feature importance and increasing model confidence. The SHAP values for every feature in every sample were calculated using the Python shap package. A feature's marginal contribution to the model's predictive output (from the baseline value to the final anticipated value) is expressed in SHAP values. The patterns of connection between these FARGs and risk for disease are demonstrated by the SHAP swarm plots. The SHAP swarm plots reveal the association patterns between these FARGs and disease risk. Model performance was quantified for the training cohort and an independent cohort using the C-statistic, Kaplan-Meier (KM) curves, and time-dependent ROC analysis, utilising the survival and survival-mining packages in R.

2.4 Survival Analysis and Time-Dependent ROC Curves

The log-rank test was utilized to determine statistical significance, and Kaplan-Meier curves were utilized to investigate overall survival differences between high- and low-risk groups. To further illustrate the effectiveness of risk classification, gene expression heatmaps, risk score distribution plots, and survival status scatter plots were created. The area under the curve (AUC) was calculated using the timeROC package (version 0.4) in evaluating the model's prediction accuracy at 1, 3, and 5 years. The model performs well in terms of prediction when the AUC is greater than 0.7. To determine if the risk score may function as an independent prognostic factor and is independent of clinical and pathological criteria involving T-stage, age, and tumor grade, univariate and multivariate Cox regression analyses took place out.

2.5 Construction and Evaluation of Receiver Operating Characteristic (ROC) Curves

Using the rms package (version 6.5-0), ROC curves were created to predict patients' 1-year, 3-year, and 5-year survival chance through the combination of the risk score along with significant clinical and

pathological data found in the independent prognostic analysis. While the clinical net benefit was calculated using decision curve analysis, the predictive consistency of the ROC curves was investigated using calibration curves (Hosmer-Lemeshow test).

2.6 Gene Set Enrichment Analysis and Immune Infiltration Analysis

To investigate and elucidate potential mechanisms of action, functional enrichment analyses were performed using the Kyoto Encyclopedia of Genes and Genomes (KEGG) and the Gene Ontology (GO). We performed KEGG analysis using the clusterProfiler R package[21]. A corrected p-value of less than 0.05 was considered statistically significant. The ESTIMATE package was used to calculate stroma scores, immune scores, and tumour purity for TCGA samples. The CIBERSORT algorithm was used to assess the relative abundance of 22 immune cell types in each sample and to compare differences in immune cell infiltration between high- and low-risk groups.

2.7 Single-cell RNA-seq Analysis and Spatial Transcriptomics Analysis

Single-cell RNA-seq data (GSE168652), comprising one cervical cancer tissue and one adjacent normal tissue (totalling 22,998 cells), were obtained from the GEO database. The 'Seurat' package was used for quality control of the single-cell sequencing data. A logFC of 0.585 and a corrected p-value of 0.05 were used as filtering criteria. The PercentageFeatureSet function was employed to calculate the percentage of mitochondrial genes, and the characteristic genes for each PCA component were plotted. Subsequently, cells were clustered, differentially expressed genes within each cluster were identified, and cell annotation was performed; the clusters were visualised using TSNE. The clusterProfiler package in R was used to identify the biological functions of marker genes in each cell population. To investigate intercellular communication, the CellChat package was employed to construct intercellular interaction networks and infer their underlying signalling mechanisms. Additionally, the Monocle algorithm was implemented to rebuild developmental paths for several cell types. Additionally, the 10×Visium database consisted of spatial transcriptome data for CESCs. The distribution of target cells and genes was assessed using the readRDS and SCTransform packages from the Seurat program; R version 4.5.3 was used of illustrating the findings.

2.8 AI-based Drug Screening and Molecular Docking

Using Python (3.13), we calculated the 'v-score' effect size for each gene based on gene expression data from the control (Control) and disease (Treat) groups, and encapsulated these as standardised AnnData objects to serve as input for the drug repositioning tool DrugReflector. Using DrugReflector and artificial intelligence methods, we predicted disease-related drugs. The FARGs protein structures used for docking were downloaded from the AlphaFold database, whilst the 3D structures of the small molecules were obtained from the PubChem database and energy-minimised under the MMFF94 force field. This study employed AutoDock Vina 1.2.3 for molecular docking; prior to docking, hydrogenation of the receptor protein was performed using PyMol 2.5.5. Subsequently, a docking box was defined to enclose the entire protein structure. Additionally, all pre-processed small compounds and the receptor protein were converted into the PDBQT format needed for AutoDock Vina 1.2.3 docking using ADFRsuite 1.0. The global search thoroughness was set to 32 during docking, while the reverse parameters were left at their default values. The docking findings were finally visualized using PyMol 2.5.5 and Discovery Studio 2025. The docking conformation with the highest score was regarded as the binding conformation.

2.9 Statistical Analysis

Statistical analysis was performed using R software. For continuous variables, group comparisons were conducted using either Student's t-test or the Wilcoxon rank-sum test, with the specific method chosen depending on the data distribution. Associations between variables were assessed using Pearson's or

Spearman's correlation analysis. Statistical significance was defined as $P < 0.05$ or $FDR < 0.05$.

3. Results

3.1 Prognostically relevant FARGs and SHAP feature importance analysis

A univariate Cox analysis of 95 FARGs using the TCGA database identified 16 FARGs associated with prognosis (Figure 1A). We used the TCGA-CESC dataset as the training set and the GSE44001 dataset as the test set. The results from 113 machine learning algorithms indicated that, when ranked by the mean C-index, the StepCox[backward]+Enet[alpha=0.2] model exhibited the highest mean C-index for both the training and test sets; this model was therefore selected as the optimal model (Figure 1B). SHAP values reflect the contribution of each independent variable to the results of the predictive classification model, helping to elucidate the extent of influence and importance of each feature in the model's decision-making process. Therefore, we calculated the SHAP values for the StepCox[backward]+Enet[alpha=0.2] model. The bar chart of feature importance scores derived from the SHAP values (Figure 1C) indicates that TRFC has the most significant influence on the model's predictive results. We have illustrated the direction and strength of each feature's influence on the model's predictions; each point represents the SHAP value for a single sample, with colours shifting towards purple indicating higher values and towards yellow indicating lower values (Figure 1D).

3.2 Evaluation of Clinical Factors in the Prognostic Model

Patients were divided into high-risk and low-risk groups using the median risk score from the training cohort as the cut-off value. Kaplan-Meier survival analysis revealed that overall survival was significantly worse in the high-risk group compared with the low-risk group ($P < 0.001$, Figure 2A). Post-hoc analyses indicated that the model we constructed serves as an independent prognostic factor, independent of other clinical characteristics, and that the calculated risk score is an independent prognostic factor for cervical cancer (Figure 2B). To enhance predictive performance, this study combined the risk score with clinical features such as age, grade and T-stage to construct a survival plot (Figure 2C). The predictive accuracy of this nomogram was assessed using receiver operating characteristic (ROC) curves, with results showing area under the curve (AUC) values of 0.873, 0.734 and 0.803 for 1-year, 3-year and 5-year survival, respectively (Figure 2D). These findings validate the nomogram's predictive capability regarding cervical cancer prognosis. Calibration curves demonstrated that the predicted survival probabilities closely aligned with the reference line, confirming the excellent predictive accuracy of this nomogram (Figure 2E). Furthermore, we compared the expression levels of eight Ferro-ageing-related genes in tumour and normal tissues. Among these, DUOX1, E2F1, IL1B, KEAP1, SLAMF8 and TFRC were up-regulated in tumour tissues, whilst MAP3K14 was down-regulated (Figure 2F).

3.3 Functional Enrichment Analysis and Correlation with Immune Infiltration

We further conducted a GO enrichment analysis to identify the top 15 most significant terms. The GO analysis revealed the functional tendencies of differentially expressed genes across three dimensions (BP, CC and MF). Among these, BP primarily involved "lymphocyte-mediated immunity" and "leukocyte-mediated immunity" (Figure 3A); the most significant terms in CC were "T cell receptor complex" and "plasma membrane signalling receptor complex" (Figure 3B); and the top-ranked terms in MF included "antigen binding", "cytokine activity" and "cytokine receptor binding" (Figure 3C). The majority of these are related to the immune system. We also performed KEGG pathway analysis and visualised the top 15 pathways, with the most significantly correlated being "Cytokine-cytokine receptor interaction", followed by "Hematopoietic cell lineage" and "Rheumatoid arthritis" (Figure 3D). ESTIMATE analysis indicated that the risk score was negatively correlated with the immune score, stroma score and the total

ESTIMATE score (Figure 3E). The high-risk group exhibited significantly lower immune scores, stromal scores and ESTIMATE total scores. Furthermore, analysis using the CIBERSORT package revealed that, in the high-risk group, CD8+ T-cell expression was reduced, and the expression of regulatory T cells (Tregs), activated NK cells and resting mast cells was significantly downregulated (Figure 3F). In summary, cervical cancer patients in the high-risk group may be in an immunosuppressed state.

3.4 Single-cell sequencing reveals the heterogeneity of cervical cancer cell populations and analysis of cell subpopulations associated with FARG characteristics

To elucidate the cellular composition of cervical cancer, this study analysed the single-cell RNA sequencing dataset GSE168652. Following quality control assessment, a total of 23,268 cells were identified from the single-cell transcriptomic data. Subsequently, a clustering algorithm was employed to divide these cells into 16 distinct cell clusters (Figure 4A). By analysing the gene expression profiles of each cell cluster and combining these with known cell type-specific biomarkers, we completed cell type annotation (Figure 4B). Based on these results, five major cell types were identified: epithelial cells, fibroblasts, endothelial cells, CD8+ T cells and macrophages.

Among the identified hub genes, we found that IL1B, SLAMF8, TFRC and TNFAIP3 were significantly expressed in Macrophages; TNFAIP3 was primarily expressed in CD8+ T cells; and DUOX1 and KEAP1 were primarily expressed in Epithelial cells (Figures 4C–E). To assess the correlation between the iron-ageing (FARG) risk profile constructed from bulk RNA-seq and the single-cell RNA-seq (scRNA-seq) profiles, we employed the Scissor computational analysis tool. In the GSE168652 dataset, the low-risk groups were numerous across the three cell types: 1,993 Scissor- cells and 1,820 Scissor+ cells were identified in epithelial cells; 116 Scissor- cells and 43 Scissor+ cells were identified in CD8+ T cells; and 89 Scissor- cells and 9 Scissor+ cells were identified in macrophages (Figure 4F). A scatter plot illustrates the cells in the high- and low-risk groups (Figure 4G).

3.5 Cell Trajectory Analysis

We employed pseudo-time series analysis to investigate the endothelial-to-fibroblast transition (EndMT) process in cervical cancer. The results revealed that cell differentiation exhibits a multi-branch topological structure comprising three branch nodes and two distinct cellular states (Figures 5A–B), with endothelial cells differentiating first, followed by fibroblasts. The heatmap has been ordered according to the cell differentiation process, with KEAP1 ranking first. Furthermore, as cells differentiate, the expression of MAP3K14 and TNFAIP3 decreases, whilst IL1B expression increases; TRFC and DUOX1, however, exhibit a trend of initially rising followed by a decline (Figure 5C). In the pseudo-time series analysis, the expression levels of FARGs in each cell were plotted along a pseudo-timeline to reveal the expression patterns of these genes during the dynamic differentiation process (Fig. 5D).

3.6 Analysis of Cell-Cell Communication Analysis of cell-cell communication revealed patterns of cell-cell interactions. Cell-cell interactions were more active in the low-risk group; the number of interactions was 57 in the high-risk group and 132 in the low-risk group, whilst the interaction strength was 1.752 in the high-risk group and 5.244 in the low-risk group (Figure 6A). Pathways such as VISFATIN were more active in the high-risk group, whilst pathways including MHC-I, MHC-II and SPP1 were more active in the low-risk group. CD8+ T cells are inextricably linked to MHC-I-peptide complexes; the number of CD8+ T cells was higher in the low-risk group than in the high-risk group, which is consistent with our previous findings from the immune infiltration analysis of the high- and low-risk groups (Figure 6B). The scatter plot for the high-risk group indicates that both signal transmission and reception by CD8+ T cells and macrophages are relatively weak, whereas signal transmission and reception by epithelial cells are strong. In the low-risk group, signal transmission and reception by macrophages are relatively strong

(Figure 6C). We generated a heatmap of cell-cell communication, which revealed that intercellular interactions were stronger in the low-risk group than in the high-risk group (Figure 6D). Furthermore, both the intensity and number of interactions were higher in the low-risk group than in the high-risk group (Figure 6E). We subsequently analysed the ligand-receptor pairs between epithelial cells and various cell types in the high- and low-risk groups. In the high-risk group, epithelial cells communicate with CD8+ T cells via APP–CD74 and MIF–(CD74+CXCR4). Notably, in the low-risk group of cervical cancer patients, epithelial cells exhibited a higher level of interaction with macrophages via APP–CD74 signalling (Figure 6F).

3.7 Clustering and Spatial Distribution Analysis of Spatial Transcriptomics Data To further investigate the spatial structure of the tumour microenvironment, we analysed spatial transcriptomics samples of cervical cancer from the Visium database. First, the data were clustered and the results mapped onto the sections. Unsupervised clustering identified 14 spatial clusters (Clusters 0–13) within the tissue sections, revealing significant regional transcriptional heterogeneity (Figures 7A–C) . Subsequently, the cells were annotated, primarily as epithelial cells, and the results of this annotation were mapped onto the sections (Figure 7D). Gene expression was visualised, showing that DUOX1, KEAP1, MAP3K14 and TFRC were highly expressed in cervical cancer epithelial cells; the figures also illustrated the distribution of gene expression.

3.8 AI-based drug screening and molecular docking: Based on gene expression profiles of cervical cancer and normal controls, we calculated the v-score effect size for each gene and used the DrugReflector AI tool to predict potential therapeutic drugs (Figure 8A). We performed molecular docking analyses of the top-ranked drug, BRD-A56372469, with FARGs to predict the clinical drug value of the model genes (Figure 8B). Among these, DUOX1 exhibited the lowest binding energy with BRD-A56372469, at –8.312 kcal/mol. A negative binding affinity indicates the possibility of binding; generally, the smaller the value, the greater the likelihood of binding (Table 1).

4. Discussion

Cervical cancer (CC) ranks fourth among cancers affecting women's health globally[22]. The majority of CC cases are caused by genital human papillomavirus (HPV) infection. Approximately 70–80% of CC cases are squamous cell carcinomas, 20–25% are adenocarcinomas, and the remaining cases are adenosquamous carcinomas and rare histological subtypes[23, 24]. Exploring the pathogenesis of CC and identifying new therapeutic targets are crucial for improving patient survival rates. In this study, we have, for the first time, integrated the emerging biological concept of ferro-ageing. Utilising multiple public databases and multi-omics technologies—including single-cell and spatial transcriptomics—we constructed and validated a cervical cancer prognostic risk model comprising eight ferro-ageing-related genes (DUOX1, E2F1, IL1B, KEAP1, MAP3K14, SLAMF8, TFRC and TNFAIP3). Patients in the high-risk group had much lower overall survival than those in the low-risk group, and the model showed moderate prognostic discriminating power in both the internal training set and the external validation cohort. This ferro-aging risk signature is a prognostic factor independent of clinical and pathological parameters, according to multivariate analysis. This suggests that it may be a useful addition to traditional staging and offer a new molecular tool for individualized prognostic assessment in cervical cancer.

The eight genes in this model were chosen from the intersection of cellular senescence and iron metabolism; their biological roles capture the most important amenities of the iron-senescence pathway. Transferrin receptor 1, a crucial gatekeeper for cellular iron uptake, is generated by TFRC. Abnormal overexpression of this gene may culminate in intracellular iron buildup, which promotes cellular senescence and increases vulnerability to ferroptosis through the production of high levels of reactive

oxygen species[25]. Tumor cells show increased resistance to ferroptosis and senescence when KEAP1 is defective. KEAP1 is an important oxidative stress sensor that can inhibit antioxidant responses by detrimentally impacting NRF2[26]. DUOX1 is responsible for ROS production; changes in its expression are closely associated with the accumulation of DNA damage and premature cellular ageing, and DUOX1 can mediate ferroptosis, inhibit tumour progression and alleviate oxidative stress responses[27, 28]. At the regulatory level, E2F1, as a key cell cycle transcription factor, can induce the classical senescence programme[29]; MAP3K14 activates the non-classical NF-κB pathway, working in concert with IL-1β—a core senescence-associated secretory phenotype factor—to create a pro-inflammatory microenvironment[30, 31]; whilst TNFAIP3 acts as a negative feedback regulator, finely tuning NF-κB-mediated inflammatory and survival signals, and its dysregulation may disrupt the iron-senescence balance[32-34]. SLAMF8 is primarily expressed in myeloid cells and participates in macrophage polarisation and inflammation regulation, thereby incorporating immune cells into the iron-ageing network[35, 36]. This set of genes reflects both iron-driven oxidative damage and the initiation of ageing, whilst also encompassing the accompanying pro-inflammatory secretory phenotype and immune regulatory processes, thereby providing a systemic overview of the multifaceted role of iron-ageing in the malignant progression of cervical cancer.

To gain a deeper understanding of the biological mechanisms underlying the risk characteristics of iron-related ageing, we conducted GO and KEGG enrichment analyses on the differentially expressed genes between the high-risk and low-risk groups. Biological processes were primarily enriched in ‘lymphocyte-mediated immunity’ and ‘leukocyte-mediated immunity’; the most significant cellular components were ‘T-cell receptor complexes’ and ‘plasma membrane signal receptor complexes’; and the top-ranked molecular functions included ‘antigen binding’, ‘cytokine activity’ and ‘cytokine receptor binding’. In the KEGG pathway analysis, the most significant pathway was “Cytokine-Cytokine Receptor Interaction”, followed by “Haematopoietic Cell Lineage” and “Rheumatoid Arthritis”. These results consistently point to the fact that the core of the difference in iron-related ageing risk lies in the dysregulation of the immune response and cytokine networks.

This pattern of functional enrichment has a deep mechanistic foundation when considering the biological core of iron-induced aging. Lipid peroxidation and oxidative stress induced by iron metabolism disorders are not only the core driving events of ferroptosis, but also key triggers that induce cells to enter a senescent state[37, 38]; Tumour cells and stromal cells that have entered senescence subsequently acquire a senescence-associated secretory phenotype (SASP), secreting large amounts of pro-inflammatory factors, chemokines and proteases such as IL-1β, IL-6 and TNF-α[39]. The activation of the "cytokine-cytokine receptor interaction" pathway is largely dependent on these SASP components[40, 41]. Among the model genes in this study, IL1B, as a core effector of SASP, can directly drive the cascade activation of the aforementioned cytokine network, whilst MAP3K14 continuously maintains the SASP transcriptional programme via the non-classical NF-κB pathway[42, 43]. Previous studies have indicated that the NF-κB signalling pathway is the primary pathway stimulating the emergence of SASP, whilst iron-induced oxidative stress can similarly promote the establishment of SASP by activating NF-κB, forming a positive feedback loop of iron metabolism disruption—oxidative stress—ageing—SASP—inflammation[44]. Concurrently, iron accumulation in the tumor microenvironment can cause ferroptosis and malfunction in $CD8^+$ T cells, suggesting that the iron-overloaded tumor microenvironment itself can directly hinder adaptive immunity. Tumor-derived ferritin and T-cell receptor hyperactivation work together to downregulate the iron efflux protein SLC40A1 in $CD8^+$ T cells, causing intracellular iron buildup and lipid peroxidation[45]. TFRC, the central gene in this model, has been connected to

dysregulated immune cell infiltration and a poor prognosis in cervical cancer. Additionally, it directly backs up this process of iron uptake[25]. Tumor cells can evade immune surveillance by developing ferroptosis resistance through the NRF2-NQO1 axis as a result of KEAP1 functional loss[46]. Therefore, the disruption of immune-related pathways seen in the high-risk group is a broader transcriptional-level manifestation of the interaction between cellular senescence, iron metabolism dysregulation, and the senescence-associated secretory phenotype (SASP), rather than simply expressing distinctions in immune status between risk groups.

Building on this, the ESTIMATE analysis further demonstrated that the risk score was significantly negatively correlated with the immune score, the stroma score and the ESTIMATE total score; all of these scores were markedly lower in the high-risk group. CIBERSORT analysis of immune cell infiltration revealed a significant reduction in the proportion of anti-tumour effector cells, such as $CD8^+$ T cells and activated NK cells, in the high-risk group, whilst regulatory T cells and quiescent mast cells also showed a downward trend. In the specific context of cervical cancer, this finding is highly consistent with existing research: senescent cells and their senescence-associated secretory phenotype (SASP) can reshape the cervical cancer tumour microenvironment by secreting various chemokines and immunoregulatory factors, thereby influencing anti-tumour immunity and tumour development[46-49]. In cervical cancer, patients in the low-risk group exhibit higher levels of SASP markers and immune cell infiltration, as well as a more active immune response, whereas an iron-overloaded microenvironment can directly weaken the core forces of anti-tumour immunity[49]. Consequently, the immunosuppressive state observed in the high-risk group—characterised by reduced overall immune infiltration and a deficiency of effector immune cells—can be interpreted as the result of multidimensional immune evasion driven by iron-mediated senescence: on the one hand, iron-catalysed oxidative damage and the activation of senescence programmes prompt tumour and stromal cells to continuously release immunoregulatory factors via the SASP, whilst a chronic, low-grade inflammatory environment paradoxically leads to the expansion of myeloid suppressor cells[50]; on the other hand, the iron-overloaded microenvironment directly depletes the effector cell pool by inducing ferroptosis in $CD8^+$ T cells; simultaneously, high TFRC expression promotes iron uptake by tumour cells to maintain their proliferative and metabolic advantage, whilst abnormal DUOX1 expression disrupts the redox homeostasis of epithelial cells and may accelerate their senescence transition[51, 52]. Under the dual pressures of iron and senescence, tumour cells, immune cells and stromal cells collectively shape a deeply immunosuppressive niche, thereby undermining the host's anti-tumour immune surveillance.

An in-depth analysis of the tumour microenvironment has revealed a close association between the risk profile of iron senescence and the immune landscape. The high-risk group exhibits a marked state of immune suppression, which may be linked to abnormal SASP induced by iron senescence—persistent low-grade inflammation actually promotes the recruitment of myeloid suppressor cells and regulatory T cells, leading to the functional exhaustion of CD8+ T cells[53]. Using the Scissor algorithm, we coupled single-cell-level cellular heterogeneity with population-level risk scores, identifying macrophages, epithelial cells and CD8+ T cells as key actors in cervical cancer progression. In the high-risk group, these cell populations may transform into pro-tumour M2 macrophages, iron-ageing epithelial cells and T cells with impaired effector function, respectively, collectively erecting a multi-layered barrier of immune suppression. Spatial transcriptomics further confirmed in situ that genes associated with the iron senescence model are primarily localised to epithelial cell regions. We visualised the expression levels of FARGs along their trajectories, and spatial transcriptomics confirmed the highest probability of these genes' presence. Additionally, unique spatial communication patterns were observed in the low-risk

group. We successfully constructed a multi-branching EndMT trajectory that originates from endothelial cells and differentiates into fibroblasts. Gene heatmaps revealed a complex transcriptional programme with KEAP1 as a potential central regulatory hub, characterised by downregulation of MAP3K14/TNFAIP3, upregulation of IL1B, and transient activation of TFRC/DUOX1. Furthermore, the pseudo-temporal atlas of FARGs seamlessly integrates the clue of ferroptosis into this dynamic differentiation process, suggesting that the fine-tuning of iron metabolism and redox balance may be a crucial step in the successful progression of EndMT[54].

Of particular note is the overall enhancement of intercellular communication within the tumour microenvironment of the low-risk group, with signal transduction from epithelial cells to macrophages via the APP-CD74 pathway being particularly prominent. APP, a transmembrane protein expressed in tumour epithelial cells, binds to CD74 on the surface of macrophages[55]. Previous research in neuroimmunology has indicated that the APP-CD74 interaction can regulate the survival and inflammatory response of microglia[56]. In the low-risk microenvironment of cervical cancer, this enhanced epithelial-macrophage dialogue may steer macrophages towards an immune-surveillance rather than an immune-suppressive phenotype, thereby maintaining adaptive anti-tumour immunity, curbing tumour progression, and conferring a prognostic advantage to patients[57, 58]. This finding not only reveals the molecular mechanisms underlying microenvironmental remodelling in the iron-ageing risk model but also provides potential targets for intervention to modulate epithelial-immune interactions and improve prognosis.

AI-assisted virtual screening revealed that the small molecule BRD-A56371469 had the most potential to bind to DUOX1 in terms of therapeutic investigation. DUOX1, an enzyme that produces reactive oxygen species, is essential for controlling cellular redox equilibrium and the aging process. This drug may open up a new treatment approach that targets the iron-induced senescence signaling pathway if it disrupts the pro-tumor redox balance or restores the sensitivity of tumor cells to iron-induced senescence via modifying DUOX1 activity. Naturally, additional in vitro and in vivo testing is needed to confirm its pharmacodynamic and toxicological characteristics.

This study also has certain limitations. Firstly, the model was constructed using publicly available sequencing data; population bias and the retrospective nature of the study are therefore unavoidable, and its generalisability requires further testing in large prospective cohorts and across different ethnic groups. Secondly, although the concept of iron-driven senescence has been demonstrated in primates, direct experimental evidence regarding its molecular pathways and dynamic evolution in human cervical cancer tissues remains lacking. Furthermore, the functional synergy among the eight model genes requires causal validation through gene editing and animal models. The specific functions of the APP-CD74 signalling axis and its downstream effects require elucidation via co-culture systems and in situ functional experiments. Finally, although BRD-A56371469 has been preliminarily identified as a candidate compound, its affinity, selectivity and in vivo antitumour activity require systematic evaluation through subsequent medicinal chemistry and pharmacology studies.

In conclusion, by combining a multi-level molecular portrait of iron senescence with intercellular communication and immune microenvironment remodeling into a cohesive analytical framework, this study has built a strong prognostic profile for cervical cancer. This has given rise to a new understanding of the dual role of iron senescence in promoting carcinogenesis and facilitating immune evasion in cervical cancer. Additionally, this integrative approach acts as a model for focused intervention research and precision subtyping of tumors caused by equally intricate biological processes.

5. Conclusion

In summary, this study established and validated a novel eight-gene ferro-aging-related (FARG) prognostic signature—comprising DUOX1, E2F1, IL1B, KEAP1, MAP3K14, SLAMF8, TFRC, and TNFAIP3—which demonstrated moderate yet robust discriminatory power for cervical cancer in both internal and external cohorts. The high-risk group was characterized by an immunosuppressive tumor microenvironment. By integrating single-cell and spatial transcriptomics, we delineated critical roles of macrophages, epithelial cells, and $CD8^+$ T cells in CESC progression, revealed the dynamic expression landscape of FARGs along the endothelial-to-mesenchymal transition (EndMT) trajectory, and identified enhanced APP-CD74 signaling from epithelial cells to macrophages in the low-risk group. Furthermore, AI-assisted virtual screening and molecular docking nominated BRD-A56371469 as a candidate compound targeting DUOX1. Collectively, the FARG signature serves as a robust independent prognostic indicator for CESC. This integrated multi-omics framework not only deepens the understanding of ferro-aging biology in tumor progression but also provides a promising avenue for precision prognostication and therapeutic exploration.

Declarations

Ethics approval and consent to participate

Not applicable

Consent for publication

Not applicable

Availability of data and materials

The datasets used during the present study are available from the corresponding authors upon reasonable request.

Ethics declarations

Ethics approval and consent to participate

Not applicable.

Consent for publication

Not applicable.

Competing interests

The authors declare no competing interests.

Funding

This research received no specific grant from any funding agency in the public, commercial, or not-for-profit sectors.

Contributions

Zhengchao Yan and Sijuan Tang contributed equally to this work. Naqiu Yin and Ying Wan conceived and designed the study. Yufei Pan and Ximei Huang contributed to performing the experiments and developing methodology. Yue Li provided imaging interpretation, evaluation. Zhengchao Yan and Sijuan Tang contributed to the writing, reviewing, and revision of the paper. Jianlin Chen and Liwu Zhang acquired funding and supervised the study. All authors read and approved the final version of the manuscript.

References

1. Li Y, Deng J, Liu Y, Yu S: **HPV infection and the immune microenvironment in cervical cancer**. *Front Immunol* 2025, **16**:1645019.
2. Foley OW, Strom D, Hinchcliff EM: **Advances in Cervical Cancer**. *Hematol Oncol Clin North Am* 2025, **39**(6):1121-1137.

3. Kessler TA: **Cervical Cancer: Prevention and Early Detection**. *Semin Oncol Nurs* 2017, **33**(2):172-183.
4. Janicek MF, Averette HE: **Cervical cancer: prevention, diagnosis, and therapeutics**. *CA Cancer J Clin* 2001, **51**(2):92-114; quiz 115-118.
5. Fant C, Tewari K: **Eradicating cervical cancer in the poorest regions of the world**. *Curr Opin Obstet Gynecol* 2026, **38**(1):6-13.
6. Senthilkumar S, Chitale RA, Kempaiah P, Saraf D, Durvasula R: **Eliminating Cervical Cancer in India: Challenges and Prospects**. *Am J Trop Med Hyg* 2026, **114**(1):6-9.
7. Dijkstra MG, Snijders PJ, Arbyn M, Rijkaart DC, Berkhof J, Meijer CJ: **Cervical cancer screening: on the way to a shift from cytology to full molecular screening**. *Ann Oncol* 2014, **25**(5):927-935.
8. Curty G, de Carvalho PS, Soares MA: **The Role of the Cervicovaginal Microbiome on the Genesis and as a Biomarker of Premalignant Cervical Intraepithelial Neoplasia and Invasive Cervical Cancer**. *Int J Mol Sci* 2019, **21**(1).
9. Lin Z, Zhou Y, Liu Z, Nie W, Cao H, Li S, Li X, Zhu L, Lin G, Ding Y *et al*: **Deciphering the tumor immune microenvironment: single-cell and spatial transcriptomic insights into cervical cancer fibroblasts**. *J Exp Clin Cancer Res* 2025, **44**(1):194.
10. Wang T, Zhang L, Mei S, Wang B, Liu J, Yang W, Liao J, Wang C: **Single-cell RNA sequencing highlights the unique tumor microenvironment of small cell neuroendocrine cervical carcinoma**. *J Transl Med* 2025, **23**(1):19.
11. Wang L, Ouyang Y, Zhao Q, Wang T, Lin C: **The Mechanism of Mg(2+)-Mediated Inhibition of Cervical Cancer by Inducing a Senescence-like State via the ATM/CHK2/p21 Signaling Pathway**. *Int J Mol Sci* 2026, **27**(10).
12. Liu L, Zheng Z, You W, Yang P, Wen Y, Qiao Y, Ma S, Zhang H, Zhang S, Xu G *et al*: **Vitamin C inhibits ACSL4 to alleviate ferro-aging in primates**. *Cell Metab* 2026, **38**(4):673-693.e617.
13. Childs BG, Durik M, Baker DJ, van Deursen JM: **Cellular senescence in aging and age-related disease: from mechanisms to therapy**. *Nat Med* 2015, **21**(12):1424-1435.
14. Victorelli S, Salmonowicz H, Chapman J, Martini H, Vizioli MG, Riley JS, Cloix C, Hall-Younger E, Machado Espindola-Netto J, Jurk D *et al*: **Apoptotic stress causes mtDNA release during senescence and drives the SASP**. *Nature* 2023, **622**(7983):627-636.
15. Picos A, Seoane N, Campos-Toimil M, Viña D: **Vascular senescence and aging: mechanisms, clinical implications, and therapeutic prospects**. *Biogerontology* 2025, **26**(3):118.
16. Rajagopalan S, Long EO: **Cellular senescence induced by CD158d reprograms natural killer cells to promote vascular remodeling**. *Proc Natl Acad Sci U S A* 2012, **109**(50):20596-20601.
17. Yun MH, Davaapil H, Brockes JP: **Recurrent turnover of senescent cells during regeneration of a complex structure**. *Elife* 2015, **4**.
18. Tiwari P, Shukla SK, Rastogi Verma S: **Unraveling senescence in cancer: mechanistic complexities and therapeutic opportunities**. *Mol Biol Rep* 2025, **52**(1):521.
19. Sutanto H, Ahkami A, Fetarayani D, Romadhon PZ: **A narrative review of therapy-induced senescence in cancer: mechanisms, immune interplay, and therapeutic opportunities**. *J Egypt Natl Canc Inst* 2025, **37**(1):78.

20. Wan X, Wang X, Liu Y, Hong L, Zhao Z, Guo P: **Ferroptosis in human reproductive tract infections and associated disorders: mechanisms and emerging therapeutic opportunities**. *Front Immunol* 2025, **16**:1713074.
21. Kanehisa M, Furumichi M, Sato Y, Kawashima M, Ishiguro-Watanabe M: **KEGG for taxonomy-based analysis of pathways and genomes**. *Nucleic Acids Res* 2023, **51**(D1):D587-d592.
22. Arbyn M, Weiderpass E, Bruni L, de Sanjosé S, Saraiya M, Ferlay J, Bray F: **Estimates of incidence and mortality of cervical cancer in 2018: a worldwide analysis**. *Lancet Glob Health* 2020, **8**(2):e191-e203.
23. Castanon A, Landy R, Sasieni PD: **Is cervical screening preventing adenocarcinoma and adenosquamous carcinoma of the cervix?** *Int J Cancer* 2016, **139**(5):1040-1045.
24. Bray F, Laversanne M, Sung H, Ferlay J, Siegel RL, Soerjomataram I, Jemal A: **Global cancer statistics 2022: GLOBOCAN estimates of incidence and mortality worldwide for 36 cancers in 185 countries**. *CA Cancer J Clin* 2024, **74**(3):229-263.
25. Wang H, Zhou J, Zhang J, Yao W, Li H, Xu K, Cheng H: **LOXL1-AS1 suppresses ferroptosis in cervical cancer through m6A-dependent regulation of TFRC**. *J Mol Histol* 2025, **56**(5):320.
26. Liao Y, Chen J, Zhao Y, Yao H, Ye W, Tang H, He Z, Sheng Y, Lu S, Hu Y *et al*: **The novel Nrf2 agonist neobavaisoflavone attenuates periodontitis by inhibiting osteoclastogenesis through iron homeostasis regulation and senescence suppression**. *Free Radic Biol Med* 2026, **245**:168-184.
27. Schiffers C, Lundblad LKA, Hristova M, Habibovic A, Dustin CM, Daphtary N, Aliyeva M, Seward DJ, Janssen-Heininger YMW, Wouters EFM *et al*: **Downregulation of DUOX1 function contributes to aging-related impairment of innate airway injury responses and accelerated senile emphysema**. *Am J Physiol Lung Cell Mol Physiol* 2021, **321**(1):L144-l158.
28. Luo M, Wang Y, Liu X, Liu L, Zhu L, Chen G, Ye Q, He C, Xiao X, Li J: **Geniposide Suppresses Tumor Progression Through DUOX1-Mediated Ferroptosis in Hepatocellular Carcinoma**. *Am J Chin Med* 2025, **53**(5):1573-1589.
29. Wei S, Ma X, Liang G, He J, Wang J, Chen H, Lu W, Qin H, Zou Y: **The role of circHmbox1(3,4) in ferroptosis-mediated cognitive impairments induced by manganese**. *J Hazard Mater* 2024, **476**:135212.
30. Hartman ML, Rogut M, Mielczarek-Lewandowska A, Wozniak M, Czyz M: **17-Aminogeldanamycin Inhibits Constitutive Nuclear Factor-Kappa B (NF-κB) Activity in Patient-Derived Melanoma Cell Lines**. *Int J Mol Sci* 2020, **21**(11).
31. Hong Y, Heo J, Kang S, Vu TH, Lillehoj HS, Hong YH: **Exosome-mediated delivery of gga-miR-20a-5p regulates immune response of chicken macrophages by targeting IFNGR2, MAPK1, MAP3K5, and MAP3K14**. *Anim Biosci* 2023, **36**(6):851-860.
32. Chen J, Wang Z, Du Y, Liu B, Chen Y, Chen G, Cui W: **Injectable CRISPRa-microspheres for targeted A20 activation rescue age-related osteogenic impairment via senescence mitigation**. *Biomaterials* 2026, **328**:123830.
33. Smith MA, Culver-Cochran AE, Adelman ER, Rhyasen GW, Ma A, Figueroa ME, Starczynowski DT: **TNFAIP3 Plays a Role in Aging of the Hematopoietic System**. *Front Immunol* 2020, **11**:536442.

34. Mooney EC, Sahingur SE: **The Ubiquitin System and A20: Implications in Health and Disease**. *J Dent Res* 2021, **100**(1):10-20.
35. Han X, Bai X, Wang N, Sun Y, Hu J, Li L, Liu Z, Zhang Y, Liang Z, Sang L *et al*: **Inhibiting SLAMF8 modulates tumor-associated macrophages and restores CD8+ T cell-mediated antitumor immunity in colorectal cancer**. *Oncoimmunology* 2025, **14**(1):2581910.
36. Wang G, van Driel BJ, Liao G, O'Keeffe MS, Halibozek PJ, Flipse J, Yigit B, Azcutia V, Luscinskas FW, Wang N *et al*: **Migration of myeloid cells during inflammation is differentially regulated by the cell surface receptors Slamf1 and Slamf8**. *PLoS One* 2015, **10**(3):e0121968.
37. Xie T, Yao L, Li X: **Advance in Iron Metabolism, Oxidative Stress and Cellular Dysfunction in Experimental and Human Kidney Diseases**. *Antioxidants (Basel)* 2024, **13**(6).
38. Huang M, Liu M, Liu J, Zhu D, Tang Q, Jia R, Chen S, Zhao X, Yang Q, Wu Y *et al*: **Functional characterization of Fur in iron metabolism, oxidative stress resistance and virulence of Riemerella anatipestifer**. *Vet Res* 2021, **52**(1):48.
39. Wang B, Han J, Elisseeff JH, Demaria M: **The senescence-associated secretory phenotype and its physiological and pathological implications**. *Nat Rev Mol Cell Biol* 2024, **25**(12):958-978.
40. Maus M, López-Polo V, Mateo L, Lafarga M, Aguilera M, De Lama E, Meyer K, Sola A, Lopez-Martinez C, López-Alonso I *et al*: **Iron accumulation drives fibrosis, senescence and the senescence-associated secretory phenotype**. *Nat Metab* 2023, **5**(12):2111-2130.
41. Ohtani N: **The roles and mechanisms of senescence-associated secretory phenotype (SASP): can it be controlled by senolysis?** *Inflamm Regen* 2022, **42**(1):11.
42. Cheng Z, Gao H, Shi P, Zhang A, Chen X, Chen Y, Gan W, Zhao K, Li S, Yang C *et al*: **Chaperone-mediated autophagy directs a dual mechanism to balance premature senescence and senolysis to prevent intervertebral disc degeneration**. *Bone Res* 2025, **13**(1):62.
43. Zhang X, Chen H, Pang T, Liang K, Mei J, Zhu Y, Yang J: **A preliminary study of sirtuin-1 on angiotensin II-induced senescence and inflammation in abdominal aortic aneurysms**. *Cytojournal* 2024, **21**:32.
44. Herbstein F, Sapochnik M, Attorresi A, Pollak C, Senin S, Gonilski-Pacin D, Ciancio Del Giudice N, Fiz M, Elguero B, Fuertes M *et al*: **The SASP factor IL-6 sustains cell-autonomous senescent cells via a cGAS-STING-NFκB intracrine senescent noncanonical pathway**. *Aging Cell* 2024, **23**(10):e14258.
45. Zhang Y, Yu R, Li Q, Song S, Fu Y, Shen X, Xu T, Zhang Y, Liang J, Zhang Z *et al*: **Epigenetic suppression of Nrf2-Slc40a1 axis induces ferroptosis and enhances immunotherapy in pancreatic cancer**. *J Immunother Cancer* 2025, **13**(10).
46. Li S, Cui Y, Zheng S, Yan Y, Jin Y, Chen Y, Yu J, Li Y, Feng L: **Multi-omics analysis reveals Yishen Qutong formula promotes ferroptosis in Lewis lung cancer associated with Keap1/Nrf2/Nqo1 pathway modulation**. *J Ethnopharmacol* 2026, **364**:121469.
47. Shao H, Li X, Wu P, Chen Z, Zhang C, Gu H: **A Cellular Senescence-Related Signature Predicts Cervical Cancer Patient Outcome and Immunotherapy Sensitivity**. *Reprod Sci*

2023, **30**(12):3661-3676.
48. Meyer M, Fourie C, van der Merwe H, Botha H, Engelbrecht AM: **Targeting treatment resistance in cervical cancer: A new avenue for senolytic therapies**. *Adv Med Sci* 2025, **70**(1):33-43.
49. Brown RAM, Richardson KL, Kabir TD, Trinder D, Ganss R, Leedman PJ: **Altered Iron Metabolism and Impact in Cancer Biology, Metastasis, and Immunology**. *Front Oncol* 2020, **10**:476.
50. Zhu W, Cheng X, Xu P, Gu Y, Xu H, Xu J, Wang Y, Zhang LW, Wang Y: **Radiotherapy-Driven Nanoprobes Targeting for Visualizing Tumor Infiltration Dynamics and Inducing Ferroptosis in Myeloid-Derived Suppressor Cells**. *J Am Chem Soc* 2024, **146**(32):22455-22468.
51. Ma X, Xiao L, Liu L, Ye L, Su P, Bi E, Wang Q, Yang M, Qian J, Yi Q: **CD36-mediated ferroptosis dampens intratumoral CD8(+) T cell effector function and impairs their antitumor ability**. *Cell Metab* 2021, **33**(5):1001-1012.e1005.
52. Kim H, Villareal LB, Liu Z, Haneef M, Falcon DM, Martin DR, Lee HJ, Dame MK, Attili D, Chen Y *et al*: **Transferrin Receptor-Mediated Iron Uptake Promotes Colon Tumorigenesis**. *Adv Sci (Weinh)* 2023, **10**(10):e2207693.
53. Salminen A, Kauppinen A, Kaarniranta K: **Myeloid-derived suppressor cells (MDSC): an important partner in cellular/tissue senescence**. *Biogerontology* 2018, **19**(5):325-339.
54. Ji HZ, Chen L, Ren M, Li S, Liu TY, Chen HJ, Yu HH, Sun Y: **CXCL8 Promotes Endothelial-to-Mesenchymal Transition of Endothelial Cells and Protects Cells from Erastin-Induced Ferroptosis via CXCR2-Mediated Activation of the NF-κB Signaling Pathway**. *Pharmaceuticals (Basel)* 2023, **16**(9).
55. Yan S, Luo M, Zhou R, Peng F, Zhang M, Feng Y, Zhao L, Yang L, Cheng Y: **Sodium-glucose cotransporter 2 inhibitors alleviate renal fibrosis in diabetic kidney disease by inhibiting Hmgcs2 and Btg2 in proximal tubular cells**. *J Transl Med* 2025, **23**(1):959.
56. Qiao Z, Wang Y, Ma X, Zhang X, Wu J, Li A, Wang C, Xiu X, Zhang S, Lang X *et al*: **GPX1 and RCN1 as New Endoplasmic Reticulum Stress-Related Biomarkers in Multiple Sclerosis Brain Tissue and Their Involvement in the APP-CD74 Pathway: An Integrated Study Combining Machine Learning and Multi-Omics**. *Int J Mol Sci* 2025, **26**(13).
57. Jiang W, Chen Y, Yu CY, Zou B, Lu Y, Yang Q, Tang Z, Mao W, Li J, Han H *et al*: **Alveolar epithelial cells shape lipopolysaccharide-induced inflammatory responses and reprogramming of alveolar macrophages**. *Eur J Immunol* 2025, **55**(1):e2350378.
58. Tsai MT, Callaghan R, Ng C, Peres-Tintin L, Matthews DB, Stanford N, Ganesh K, Estes MK, Diehl GE: **Intestinal epithelial TLR5 signaling promotes barrier-supportive macrophages**. *Sci Immunol* 2026, **11**(115):eadr4057.

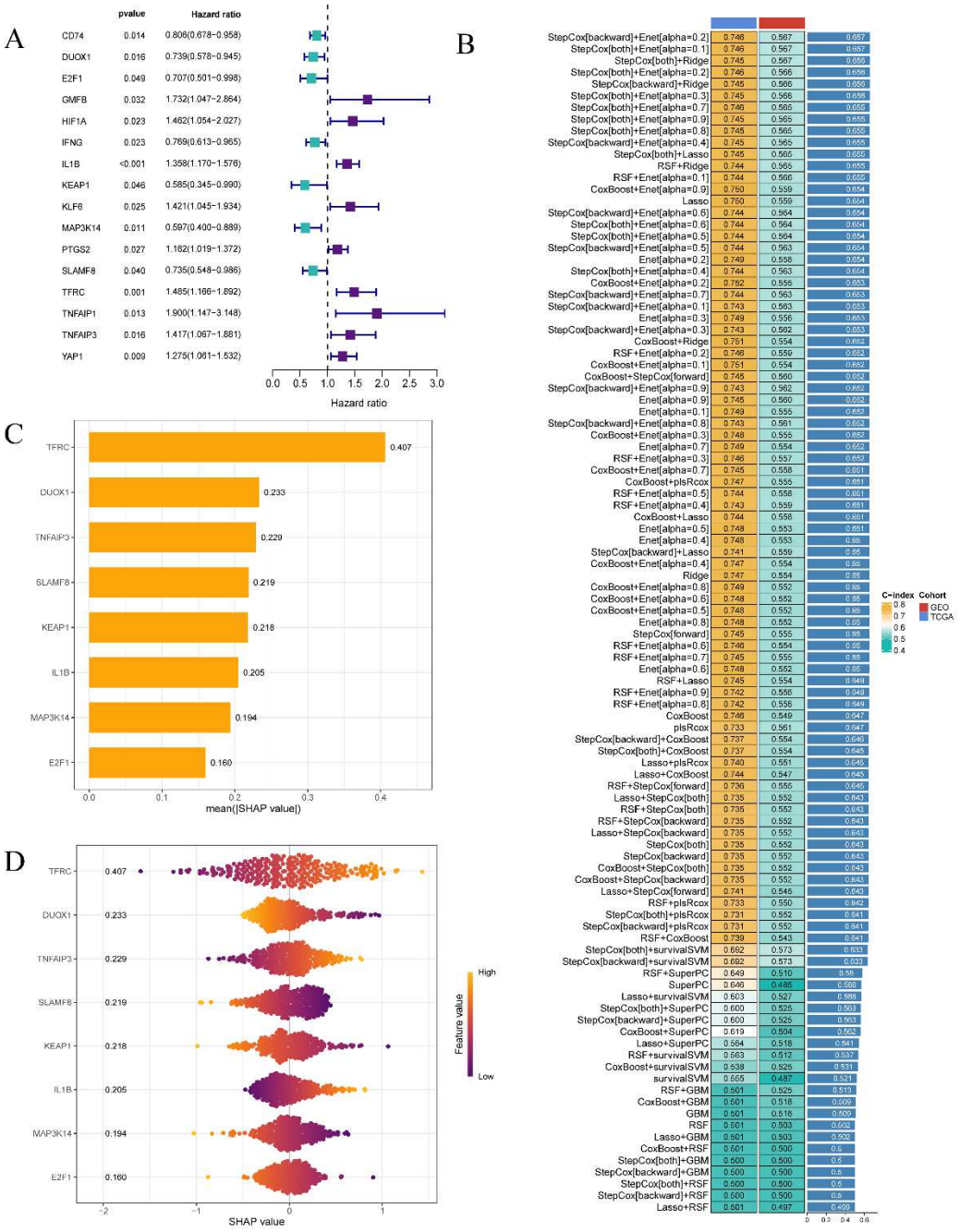


Figure 1. Biomarker identification and evaluation. (A) Forest plot of genes associated with prognosis from univariate Cox regression analysis ($P < 0.05$), showing hazard ratios (HR) and their 95% confidence intervals. (B) Combinations of 113 machine learning algorithms across two datasets. (C) Ranking of SHAP scores for variables in the model. (D) SHAP honeycomb plot for the StepCox[backward]+Enet[alpha=0.2] model.

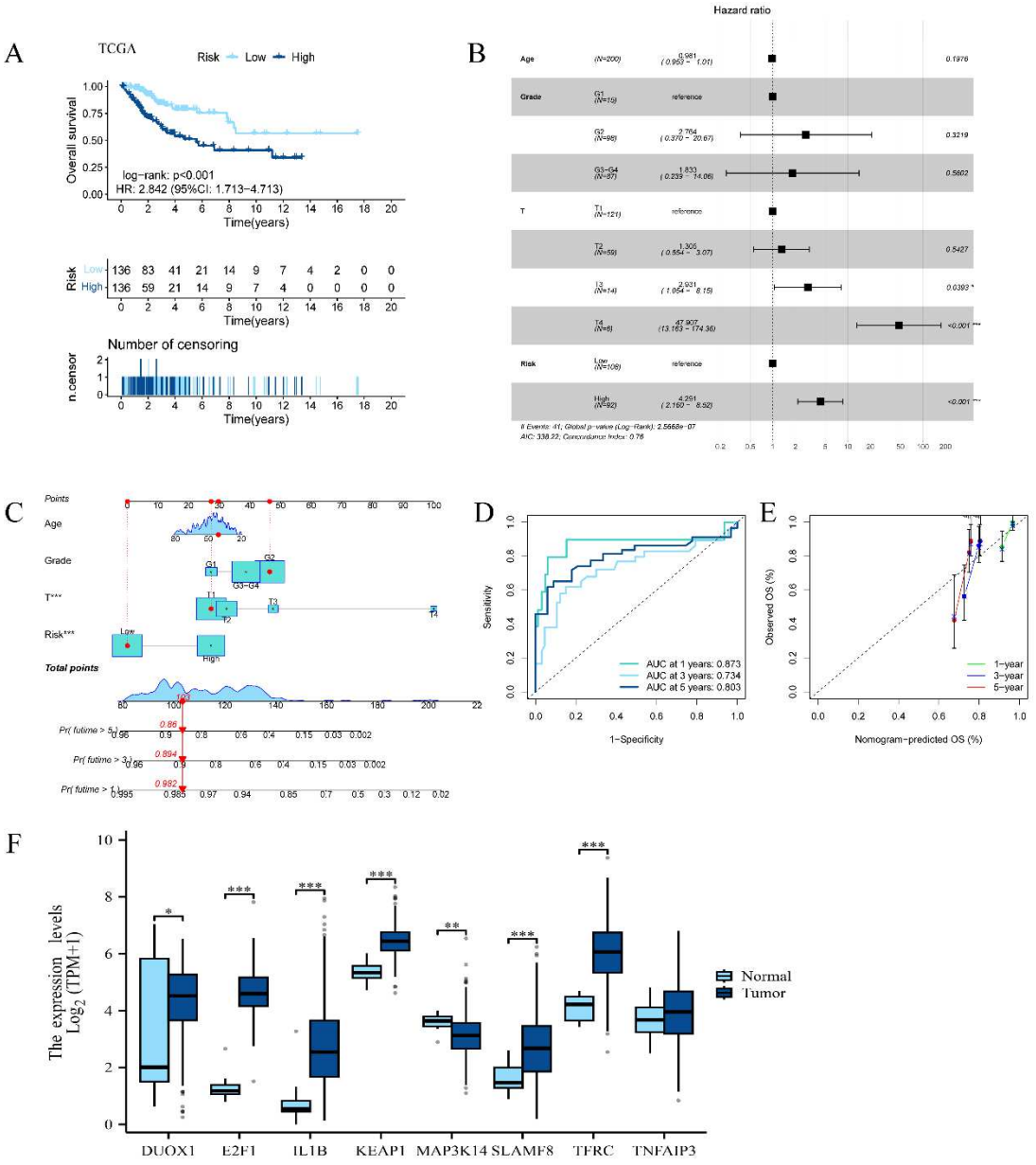


Figure 2. Clinical prognostic evaluation of FARGs. (A) Survival analysis of high- and low-risk groups of cervical cancer patients in the TCGA database. (B) Forest plot of the model's independent prognostic analysis. (C) Stacked bar chart based on risk score, age, clinical grade and T-stage. (D) ROC curve for the column plot. (E) ROC curves evaluating predictive accuracy at 1, 3 and 5 years. (F) Relative expression levels of the eight FARGs in tumour and normal tissues.

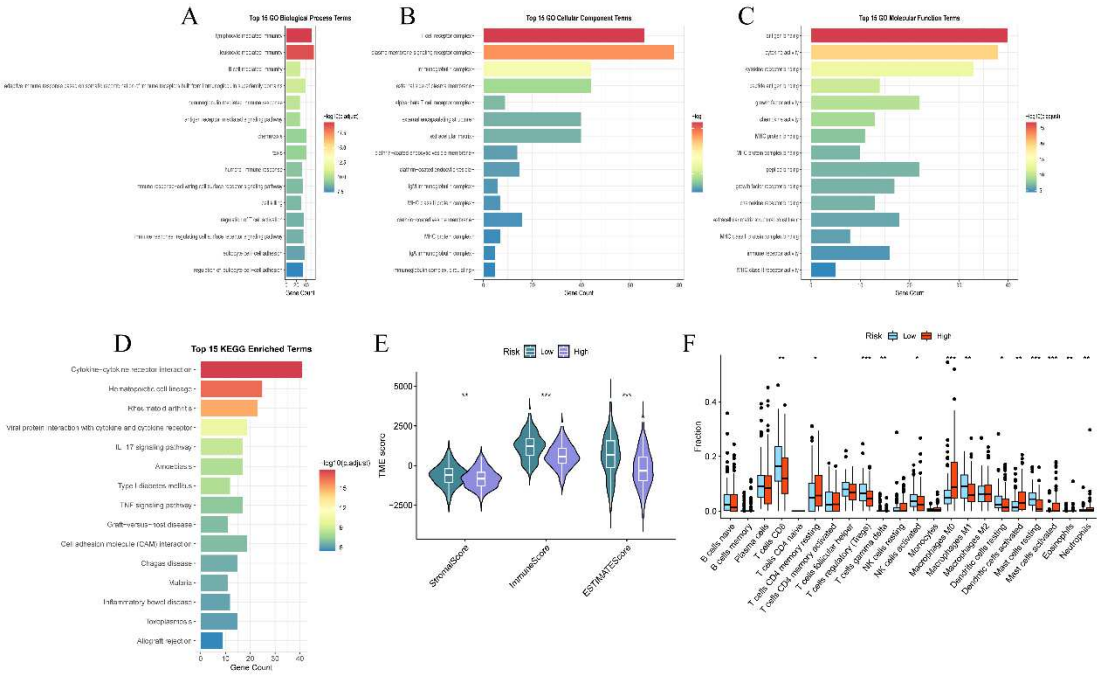


Figure 3. Functional and pathway analyses, and immune cell infiltration in high- and low-risk groups. (A) Top 15 GO biological process terms. (B) Top 15 GO cellular component terms. (C) Top 15 GO molecular function terms. (D) Top 15 KEGG-enriched terms. (E) Relative values of the immune score, stroma score and ESTIMATE score between high- and low-risk groups. (F) Relative expression levels of immune infiltrating cells between high- and low-risk groups.

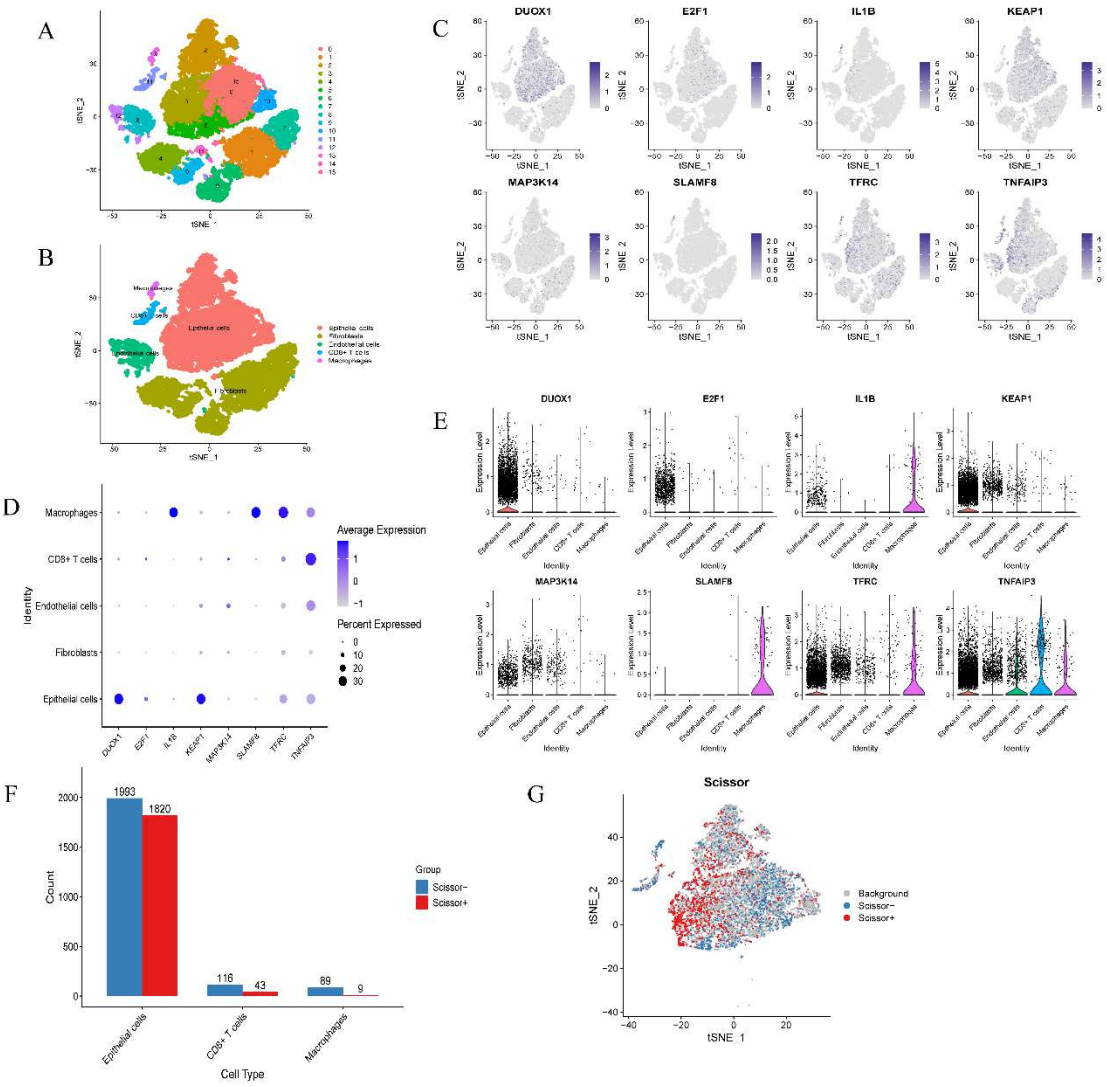


Figure 4. Identification of cellular subpopulations in cervical cancer tissue based on the single-cell sequencing dataset GSE184198. (A) A t-SNE plot showing the distribution of cervical cancer cell subpopulations. (B) A t-SNE plot presenting the annotation results for cervical cancer cell subpopulations. (C) tSNE_1 scatter plot showing the distribution of eight prognostic genes in the single-cell tumour microenvironment atlas; grey indicates low expression, blue indicates high expression. (D) Bubble plot showing genes specifically expressed in cell subpopulations. (E) Violin plot showing the expression profile of each gene. (F) Scissor analysis bar chart. The x-axis represents cell type, and the y-axis represents cell count. (G) Scatter plot of cells in the low- and high-risk groups; blue represents the low-risk group and red represents the high-risk group.

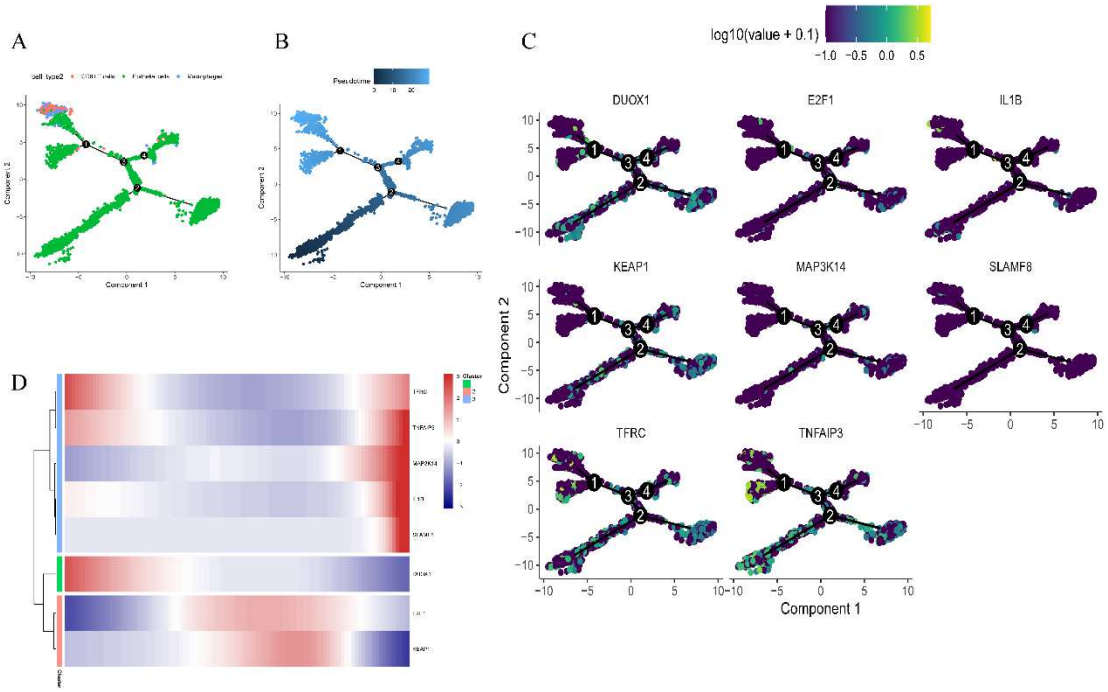


Figure 5. Pseudo-temporal analysis of EndMT in cervical cancer cells mediated by FARGs. (A–B) Reconstructed pseudo-temporal trajectories illustrating multi-branch differentiation pathways and distinct cellular states, arranged in order of developmental progression. (C) Cell trajectory heatmap. The x-axis represents cells, and the y-axis represents FARGs. Blue indicates low expression, whilst red indicates high expression. (D) Trajectory plot of FARGs.

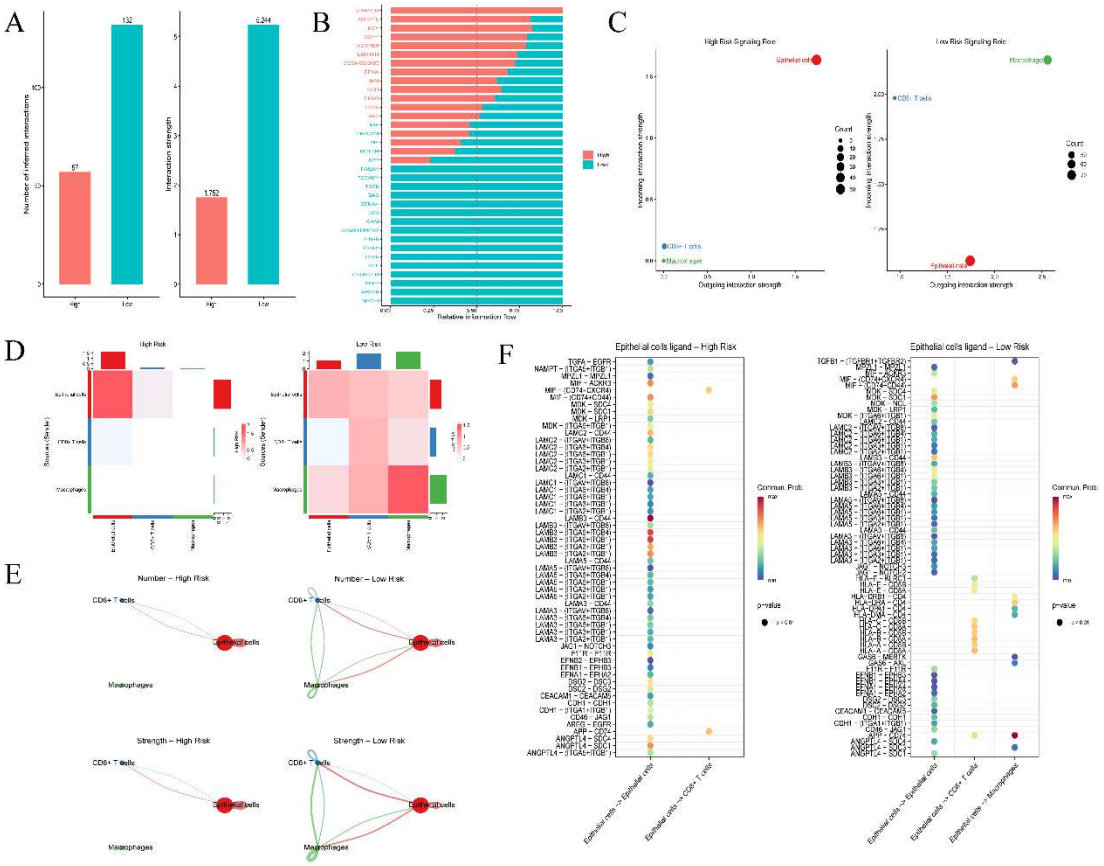


Figure 6. Analysis of intercellular communication between high- and low-FARG score groups. A. Intensity of cell-cell interactions mediated by various signalling pathways in the high- and low-FARG score groups. B. Bar chart showing the intercellular ranking of high and low FARG groups, illustrating the signal axes of the interaction networks in these groups; signal pathways marked in red are more abundantly expressed in the high FARG group, whilst those marked in light green are more enriched in the low FARG group. C. Bubble plot of intercellular communication intensity between high and low FARG groups. D. Heatmap of intercellular communication intensity, with blue and red representing weakened and enhanced intercellular communication, respectively. E shows the intercellular interaction networks in the low- and high-FARG score groups; thicker lines indicate stronger communication. F is a bubble plot of changes in intercellular communication mediated by each signalling axis, with the x-axis representing the initiating and receiving cell populations and the y-axis representing the receptor-ligand pairs of the signalling pathway.

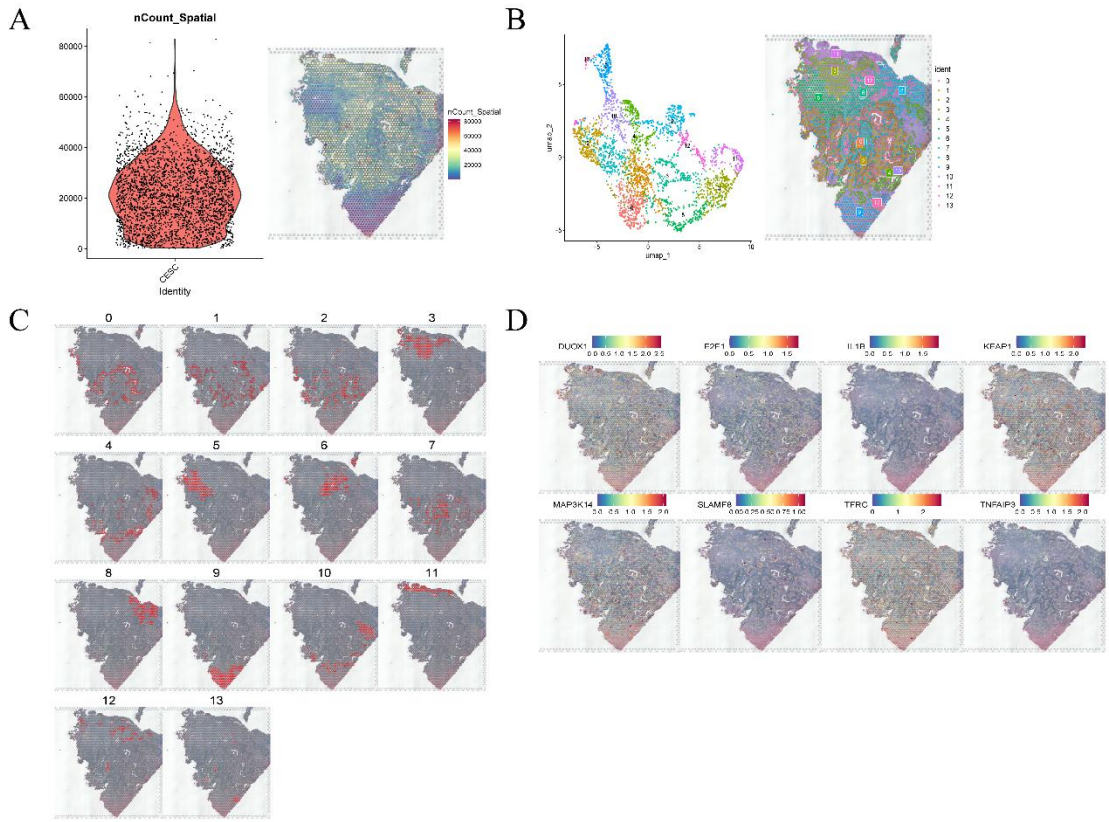


Figure 7. Distribution of FARGs in cervical cancer epithelial cells. (A) Sequencing depth plots: in the left-hand plot, the x-axis represents sample names and the y-axis represents the number of sequences detected per point; the right-hand plot shows the number of sequences mapped to the section. The deeper the red, the higher the number of sequences. (B) Clustering results on the section, showing a total of 14 spatial clusters. (C) Individual plots for the 14 clusters. (D) Expression of FARGs in epithelial cells, where blue indicates low expression and red indicates high expression.

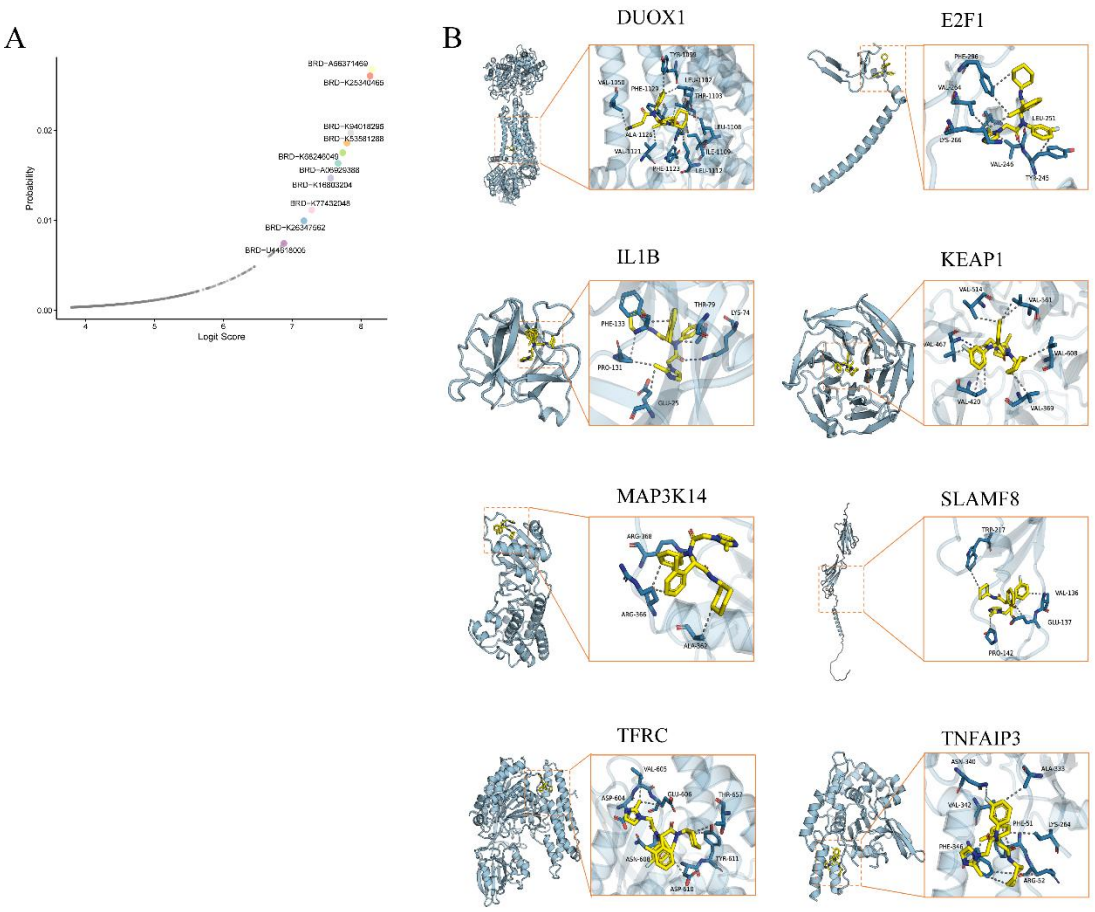


Figure 8: Drug screening and molecular docking. (A) A volcano plot of the top ten drugs, with the x-axis representing drug scores and the y-axis representing predicted likelihood. (B) Binding modes obtained from docking; the left panel shows an overall view, whilst the right panel shows a localised view. In the figure, the yellow stick model represents the small molecule, the cyan cartoon model represents the protein, the red dashed lines indicate hydrogen bonds, and the grey dashed lines indicate hydrophobic interactions.

Table 1: Connection Scoring Sheet

Target_name	Ligand_name	Docking_score(kcal/mol)
DUOX1-7D3E	BRD-A56371469	-8.312
E2F1-2AZE	BRD-A56371469	-5.409
IL1B-1I1B	BRD-A56371469	-6.922
KEAP1-1U6D	BRD-A56371469	-7.928
MAP3K14-4IDT	BRD-A56371469	-5.9
SLAMF8	BRD-A56371469	-6.842
TFRC-3KAS	BRD-A56371469	-7.429
TNFAIP3-3ZJD	BRD-A56371469	-6.505

Supplementary Files

This is a list of supplementary files associated with this preprint. Click to download.

- KEGGPERMISSION261490.pdf